Characterization of the Prefusion and Transition States of Severe Acute Respiratory Syndrome Coronavirus S2-HR2[†]

Susanna McReynolds,[‡] Shaokai Jiang,[‡] Ying Guo,[§] Jessica Celigoy,[‡] Christine Schar,[||] Lijun Rong,[⊥] and Michael Caffrey*[,‡]

Department of Biochemistry and Molecular Genetics, University of Illinois at Chicago, Chicago, Illinois 60607, Institute of Materia Medica, Peking Union Medical College and Chinese Academy of Medical Sciences, Beijing 100050, China, Center for Structural Biology, University of Illinois at Chicago, Chicago, Illinois 60607, and Department of Microbiology and Immunology, University of Illinois at Chicago, Chicago, Illinois 60612

Received April 8, 2008; Revised Manuscript Received May 6, 2008

ABSTRACT: The envelope glycoproteins of the class I family, which include human immunodeficiency virus (HIV), influenza, and severe acute respiratory syndrome coronavirus (SARS-CoV), mediate viral entry by first binding to their cellular receptors and subsequently inducing fusion of the viral and cellular membranes. In the case of SARS-CoV, heptad repeat domains of the envelope glycoprotein, termed S2-HR1 and S2-HR2, are thought to undergo structural changes from a prefusion state, in which S2-HR1 and S2-HR2 do not interact, to a postfusion state in which S2-HR1 and S2-HR2 associate to form a six-helix bundle. In the present work, the structural and dynamic properties of S2-HR2 have been characterized. Evidence is presented for an equilibrium between a structured trimer thought to represent a prefusion state and an ensemble of unstructured monomers thought to represent a novel transition state. A model for viral entry is presented in which S2-HR2 is in a dynamic equilibrium between an ensemble of unstructured monomers in the transition state and a structured trimer in the prefusion state. Conversion from the prefusion state to the postfusion state requires passage through the transition state, a state that may give insight into the design of structure-based antagonists of SARS-CoV in particular, as well as other enveloped viruses in general.

Enveloped viruses of the class I family, which include human immunodeficiency virus (HIV), influenza, and severe acute respiratory syndrome coronavirus (SARS-CoV), enter their cellular targets by first binding to the cell membrane and subsequently inducing fusion of the viral and cellular membranes (*1*). In these viruses, the subunits that bind receptors are gp120, HA1, and S1 in HIV, influenza, and SARS-CoV, respectively; the subunits that mediate membrane fusion are gp41, HA2, and S2 in HIV, influenza, and SARS-CoV, respectively (*2–4*). Based on their amino acid sequences, the viral proteins that mediate membrane fusion generally possess two heptad repeats termed HR1 and HR2, which consist of seven residue motifs (where the positions are labeled "abcdefg") possessing hydrophobic residues in the "a" and "d" positions resulting in a high propensity to form helices that interact as a coiled-coil helix (*5*). There is substantial structural information available for the HR1 and HR2 domains of viral envelope proteins. For example, high-resolution structures have been determined for HR1 and HR2 domains of HIV and SIV gp41 (*6–9*), influenza HA2 (*10–12*), and SARS-CoV S2 (*13–16*). Based on these structures, as well as those from Ebola, mouse hepatitis virus, and paramyxoviruses (*17–20*), the HR1 and HR2 domains undergo large structural changes during the membrane fusion event (*1*). In the prefusion conformation, as well as the unprocessed form, the HR2 domains are thought to self-associate as parallel trimers. Specific examples of prefusion envelope structures include influenza HA2 (*10, 12*), parainfluenza virus 5 F (*20*), and SARS-CoV S2-HR1 and -HR2 (*13, 16*). In the postfusion form, the HR1 domains self-associate as trimers and the HR2 domains associate with the HR1 domains in an antiparallel orientation to form the "six-helix bundle". Examples of postfusion envelope structures include Ebola GP2 (*17, 18*), HIV and SIV gp41 (*6–9*), influenza HA2 (*11*), human parainfluenza virus 3 F (*19*), and SARS-CoV S2 (*15, 16*). The presence of the prefusion conformation is further supported by the observation that peptides, corresponding to the HR1 and HR2 regions, often exhibit antiviral activity, presumably by binding to the prefusion conformation and thereby inhibiting formation of the postfusion conformation (*21–23*). Importantly, one such peptide corresponding to the HIV gp41 HR2, termed T20 or fuzeon, is currently used as a therapy in HIV-infected humans (*24*).

A general aspect of the viral entry model is the conformation change from the prefusion state to the postfusion state, which requires dissociation of the self-associating HR2

[†] This work was partially supported by grants from the NIH (GM068944, RR022361) and NSF (0079604).

* To whom correspondence should be addressed. Tel: (312) 996-4959. Fax: (312) 413-0353. E-mail: caffrey@uic.edu.

[‡] Department of Biochemistry and Molecular Genetics, University of Illinois at Chicago.

[§] Peking Union Medical College and Chinese Academy of Medical Sciences.

[||] Center for Structural Biology, University of Illinois at Chicago.

[⊥] Department of Microbiology and Immunology, University of Illinois at Chicago.

10.1021/bi800622t CCC: $40.75
Published on Web 06/10/2008

domains while maintaining a trimer of self-associating HR1 domains; however, very little is known about the transition from the prefusion to the postfusion state. Previous studies of SARS-CoV S2-HR2 constructs have suggested that this region contains helix and is in a monomer−trimer equilibrium (*23, 25, 26*). In the present study we have examined the structural and dynamic properties of the dissociation step of SARS-CoV S2-HR2 (residues 1141−1193 of SARS-CoV S Urbani). We find that S2-HR2 is in a dynamic equilibrium between unstructured monomers and a structured trimer in the prefusion state. We suggest that the unstructured monomeric state represents a transient intermediate or transition state that is essential for envelope-mediated viral entry. Importantly, consideration of the unstructured and structured states of HR2 may be of relevance to the design of future antiviral therapies.

EXPERIMENTAL PROCEDURES

Protein Preparation. The SARS-CoV S2-HR2 domain consisting of residues 1141−1193 was subcloned into the *Bam*HI/*Hin*dIII restriction sites of a modified pQE30-expression vector (Qiagen, Valencia, CA). The resulting construct, termed His-PG-S2-HR2, consists of an N-terminal polyhistidine tag followed by protein G (the IgG binding domain of streptococcus protein G), a TEV (tobacco etch virus) cleavage site, sequence = ENLYFQGS for removal of the expression tag, and S2-HR2. For simplicity, from here on S2-HR2 will be numbered 1−55 corresponding to residues 1141−1193 of the intact protein (the N-terminal glycine and serine residues are a cloning artifact). Protein expression of unlabeled S2-HR2 was achieved in *Escherichia coli* strain SG13009 (Qiagen). For large-scale preparations, 50 mL cultures of the appropriate strains were grown overnight at 37 °C in LB media supplemented with 100 μg/mL ampicillin and 50 μg/mL kanamycin. This culture was then used to inoculate a 1 L batch of LB media supplemented with 100 μg/mL ampicillin and 50 μg/mL kanamycin. Protein expression was induced at the full exponential growth phase (OD_{600} = 0.6) by the addition of IPTG to a final concentration of 0.8 mM; cell growth was continued for 4−5 h, and the cells were harvested by centrifugation. Protein expression of ^{15}N-labeled and ^{13}C/^{15}N-labeled S2-HR2 was achieved by growing *E. coli* strain SG13009 as previously described (*13*). Briefly, the cells were grown in 4 L of LB media at 37 °C until they reached an OD_{600} of 0.8. Subsequently, the cells were pelleted, washed once with M9 salts, resuspended in 1 L of M9 minimal media supplemented with 1 g/L $^{15}NH_4Cl$ (Martek Biosciences, Columbia, MD) and/or 4 g/L ^{13}C-glucose (Isotec, Miamisburg, OH), and set to recover in the absence of antibiotic selection. Protein expression was induced after 1 h by addition of 0.8 mM IPTG and grown for an additional 4−5 h at 37 °C. The HIS-PG-S2-HR2 fusion protein was purified from the soluble fraction using a Ni^{2+} fast-flow Sepharose column (Qiagen, Valencia, CA). The proteins were then cleaved using TEV protease and run once more over the Ni^{2+} column to remove His-PG and TEV protease, which also contains a polyhistidine tag. The flow-through fraction containing S2-HR2 was then dialyzed extensively against 10 mM $NaPO_4$, pH 7.0, and concentrated by ultrafiltration (YM3; Amicon, Billerica, MA). The purity of S2-HR2 was estimated to be >98%, based on SDS−PAGE and size exclusion chromatography. The identity of S2-HR2 was confirmed by MALDI-TOF mass spectrometry (*25*).

Sedimentation Velocity. Sedimentation velocity experiments were performed in a Beckman ProteomeLab XL-1 analytical ultracentrifuge using an An60Ti rotor at 20 °C. To test for self-association, two S2-HR2 concentrations were assayed (110 and 220 μM). Epon double-sector centerpieces were filled with 400 μL of sample and buffer (10 mM $NaPO_4$, pH 7.0) and centrifuged at 50000 rpm. Absorbance data were acquired at 280 nm with a time interval of 5 min. Buffer viscosity, protein partial specific volumes, and frictional ratios were calculated with SEDNTERP (http://www.rasmb.bbri.org/) developed by Hayes, Laue, and Philo. The data were fit using a continuous $c(s)$ Lamm equation distribution model with the program Sedfit (*27*).

CD Analysis. Circular dichroism (CD) spectra were measured on a Jasco-710 spectropolarimeter. Wavelength spectra were recorded from 190 to 260 nm in 10 mM $NaPO_4$, pH 7.0, in cells of 0.1−1 mm path length. For samples containing TFE, the above buffer was diluted with TFE and the $NaPO_4$ concentration was adjusted accordingly. In all cases, the spectra were corrected by the subtraction of a blank corresponding to the buffer. The percentage of α helix was calculated by the observed molar ellipticity at 222 nm (θ_{obs}) divided by the theoretical molar ellipticity ($[\theta_t]$), where $[\theta_t] = 40000 \times (1-4.6/N)$ and $N = 55$ (the total number of residues). The thermal stability of S2-HR2 under different buffer conditions was determined by following the change in molar ellipticity at 222 nm from 5 to 80 °C with a scan rate of 1 °C/min. The fraction of helix (F_h) was determined by the equation $F_h = ([\theta_{obs}] - [\theta_u])/([\theta_f] - [\theta_u])$, where θ_{obs} is the observed molar ellipticity at 222 nm at any given temperature, θ_f is the molar ellipticity at 222 nm at 5 °C (the folded state), and θ_u is the molar ellipticity at 222 nm at 80 °C (the unfolded state). In this analysis, the midpoint of the thermal denaturation, T_m, corresponds to the temperature where 50% of the protein has unfolded.

NMR Assignment. Backbone assignments were determined using a standard set of 3D heteronuclear NMR experiments including HNCO, HN(CO)CA, and HNCA on Bruker DRX 600 MHz and Bruker AVANCE 800 MHz spectrometers equipped with cryogenic triple resonance probes (cf. ref *13*). The side-chain resonances were assigned by 3D ^{15}N-edited TOCSY-HSQC, 3D HCC(CO)NH, and 3D CC(CO)NH experiments. 3D ^{15}N-edited NOESY-HSQC (mixing time = 120 ms) and 3D ^{13}C-edited NOESY-HSQC (mixing time = 100 ms) were acquired for distance information, as well as confirmation of side chain assignments. Experimental conditions were 400 μM S2-HR2 in 10 mM $NaPO_4$, pH 7.0, and 10% ^2H_2O at 25 °C. Spectra were processed by NmrPipe and visualized with NmrDraw (*28*).

Solvent Exchange. The H_N exchange rates are described by the equation $I/I_0 = (k_{ex}/(R_z + k_{ex} - R_z^{water}))(\exp(-R_z^{water}t_{mix}) - \exp(-(R_z + k_{ex})t_{mix})) \approx k_{ex}t_{mix}$ at short t_{mix}, where I and I_0 are the observed and reference intensities, respectively, k_{ex} is the solvent exchange rate, R_z is the H_N longitudinal relaxation rate, R_z^{water} is the water longitudinal relaxation rate, and t_{mix} is the mixing timer (*29, 30, 32*). A series of CLEANEX-PM experiments (*30*) were performed with t_{mix} = 5, 10, 15, 20, 40, 60, 80, and 100 ms. Experimental conditions were 400 μM S2-HR2 in 10 mM $NaPO_4$, pH 7.0, and 10% ^2H_2O at 25 °C. The k_{ex} were

determined from the initial slope of I/I_0 versus t_{mix} ($t_{mix} \leq$ 20 ms) using KaleidaGraph 4.0. The errors correspond to the estimated fitting errors of the linear regression. The relative exchange was calculated by k_{ex}/k_{int}, where k_{int} was estimated by the program Sphere (www.fccc.edu/research/labs/roder/sphere,31).

Inhibition of Viral Entry. HIV pseudotyped virions with SARS-CoV S protein were produced by cotransfecting the cDNA of wild-type S gene with an envelope-deficient HIV vector, pNL4-3-Luc-R-E-, into 293T cells (producer cells) by the modified $Ca_3(PO_4)_2$ method. 293T cells were transfected with 10 μg of HIV vector and 15 μg of S or VSV-G DNA. After 16 h, cells were washed once with PBS, and fresh medium was added to the plates. The pseudotyped virions in the supernatant were harvested after 48 h and filtered with a 0.45 μm pore-size filter. At 16 h posttransfection of 293T cells with human ACE2, the cells were seeded in 24-well plates and challenged with the S pseudotyped HIV viruses, which had previously been incubated with varying concentrations of S2-HR2 for 15 min at room temperature. The media was changed 16 h postinfection, and cell lysates were analyzed for luciferase activity 48 h postinfection. Luciferase activity was measured with a Berthold FB12 luminometer according to the manufacturer's instructions. Control experiments utilized HIV/VSV pseudotyped virions, which were not affected by the S2-HR2 peptide (data not shown). Each experiment was performed in triplicate from the transfection stage.

RESULTS

Oligomerization State of S2-HR2. The construct characterized herein consists of residues 1141−1193 of SARS-CoV Urbani (GenBank accession number AY278741), as shown in Figure 1a. In addition, the positions of the heptad repeats are shown. Previous characterizations of smaller S2-HR2 constructs (consisting of 37−39 residues) have shown by analytical ultracentrifugation that S2-HR2 is in an equilibrium between monomeric and trimeric forms (*23, 26*). However, a S2-HR2 construct consisting of 44 residues was shown by analytical ultracentrifugation and X-ray crystallography to be a tetramer (*16*). In Figure 1b, the sedimentation distribution of our construct of S2-HR2 (consisting of 55 residues) is shown, based on sedimentation velocity experiments. The buffer conditions were chosen to mirror those of the optimal NMR conditions discussed below (10 mM $NaPO_4$, pH 7.0 at 25 °C). At a concentration of 110 μM, we observe two dominant species at *S* values of 0.85 and 1.55, which correspond to monomer and trimer species. At this concentration, the monomer:trimer ratio is 3.6. At a concentration of 220 μM, we again observe two dominant species at *S* values of 0.87 and 1.64 and the monomer:trimer ratio is 0.72. The increased amount of trimer at higher concentration suggests an equilibrium between the monomer and trimer.

Equilibrium between Structured and Unstructured States of S2-HR2. Figure 2a shows the CD spectra of S2-HR2 in 10 mM $NaPO_4$, pH 7.0, at concentrations of 40, 400, and 1000 μM. As shown by the CD signal at 222 nm, the helix content increases with concentration. For example, at 40 μM the molar ellipticity at 222 nm is ∼−9000°, and at 1 mM the molar ellipticity at 222 nm is ∼−20200°. The correlation between concentration and helical structure suggests that S2-HR2 is in a dynamic equilibrium between structured and unstructured states. Figure 2b shows the effect of the cosolvent TFE on S2-HR2 secondary structure. As the concentration of TFE is increased from 0% to 40%, the molar ellipticity at 222 nm increases from ∼−9000°, which corresponds to ∼14 residues or 25% helix, to ∼−24500°, which corresponds to ∼37 residues or 67% helix. The stability of S2-HR2 was next probed by thermal denaturation monitored by the CD signal at 222 nm under the aqueous and cosolvent conditions. As shown by Figure 2c, S2-HR2 exhibits a T_m of 33 °C at a protein concentration of 400 μM in 10 mM $NaPO_4$, pH 7.0. This reaction is completely reversible as evidenced by subsequent scans of the same sample. In contrast, in the presence of cosolvent, the T_m of S2-HR2 increased to >60 °C (data not shown). Thus, under aqueous conditions the helical structure of S2-HR2 is relatively unstable at physiological temperatures.

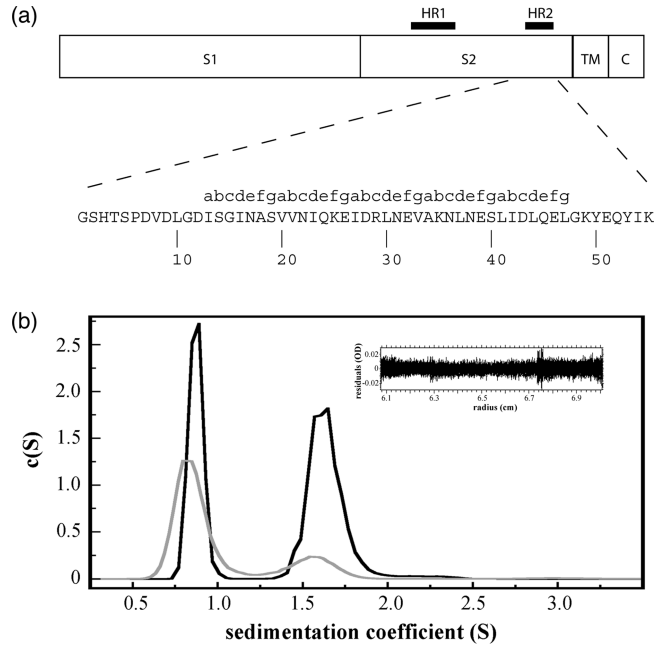

FIGURE 1: (a) Amino acid sequence of the SARS-CoV S2-HR2 construct. The sequence shown corresponds to that of SARS-CoV S Urbani (GenBank accession number AY278741). The relative position of S2-HR2 within spike is shown above. The numbering below the sequence corresponds to that of the construct characterized herein. Note that the first two residues (G and S) are cloning artifacts. The letters above the sequence correspond to the heptad repeat positions. (b) Oligomerization properties of S2-HR2, as determined by sedimentation velocity. The gray and black lines correspond to S2-HR2 concentrations of 110 and 220 μM, respectively. The inset shows the residuals for the fit of the 220 μM data to a monomer−trimer model. The buffer conditions were 10 mM $NaPO_4$, pH 7.0 at 25 °C.

Structural Properties of S2-HR2. The structural properties of S2-HR2 were further investigated by NMR spectroscopy. The optimal conditions for NMR experiments in aqueous solution (i.e., in the absence of cosolvent) were found to be 400 μM S2-HR2 in 10 mM $NaPO_4$, pH 7.0 at 25 °C. A two-dimensional ^{15}N-edited HSQC spectrum of S2-HR2 with the $^{15}N-^{1}H$ assignments is shown in Figure 3a. The backbone assignments were obtained using the standard set of three-dimensional triple resonance experiments (*13*). In all NMR experiments, the spectra show a single set of resonances indicating that the monomeric and trimeric species observed by sedimentation velocity are in fast exchange on the NMR

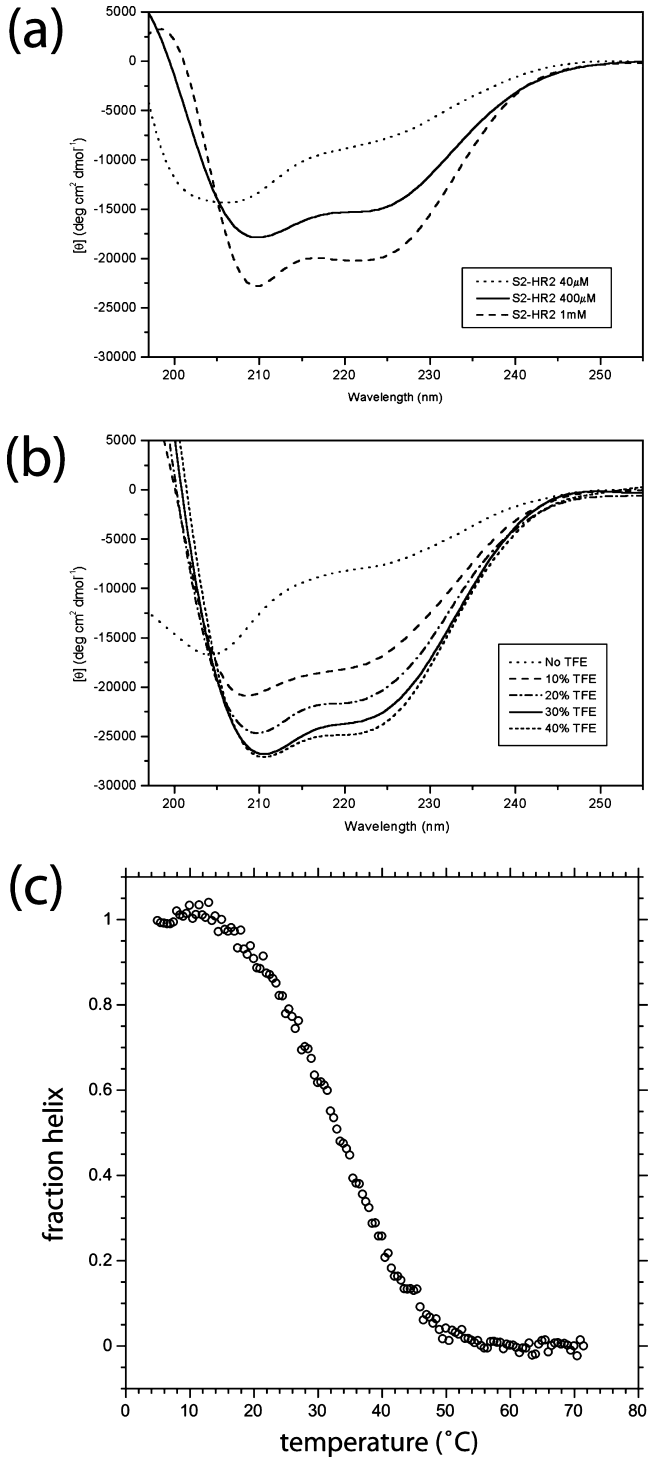

FIGURE 2: Secondary structure and stability of SARS-CoV S2-HR2 as monitored be CD. (a) CD spectra of S2-HR2 in 10 mM $NaPO_4$, pH 7.0 (23 °C), at three different concentrations of S2-HR2: 40 μM (dotted line), 400 μM (solid line), and 1 mM (dashed line). (b) CD spectra of S2-HR2 at 30 μM in 10 mM $NaPO_4$, pH 7.0 at 23 °C, with various amounts of TFE present. (c) Temperature denaturation profiles of S2-HR2 as monitored by molar ellipticity at 222 nm. Experimental conditions were 400 μM S2-HR2 in 10 mM $NaPO_4$, pH 7.0.

time scale in which a population-weighted average chemical shift is observed. The backbone chemical shifts of S2-HR2 support this notion, as shown by Figure 3b. For example, the observed $^{13}C_\alpha$ and ^{13}CO chemical shifts are indicative of a core helix from residues 18−39 of the construct, which corresponds to a helix content of ~40%. Additional helical character is suggested by the ^{13}C chemical shifts of residues 10−17 and 40−49 of the S2-HR2 construct. Note that we have previously shown that in the presence of cosolvent the helix of S2-HR2 encompasses residues 17−47 of the construct (*13*). Interestingly, the secondary chemical shift deviations of the core helix under aqueous conditions are only ~30% of the magnitude of that observed in the presence of cosolvent where S2-HR2 is a structured trimer (*13*), which is consistent with the notion that S2-HR2 is in dynamic equilibrium between unstructured monomers and a structured trimer.

Dynamic Properties of SARS-CoV S2-HR2. Protein structure and dynamic properties can be probed by the exchange rates of amide groups with solvent in which amide groups that participate in hydrogen-bonding networks (e.g., regions of helix or β-sheet structure) exhibit slower exchange rates than amide groups that do not participate in hydrogen bonds. Accordingly, the structural and dynamic properties of S2-HR2 were probed by CLEANEX-PM NMR experiments, which measure the exchange rates of amide groups with solvent on the millisecond time scale (*30*). As shown by Figure 4a, the presence of nearly all $^1H-^{15}N$ correlations in this experiment suggest that the majority of S2-HR2 amide groups are exchanging with H_2O on the 100 ms time scale in the absence of cosolvent, indicating that they do not participate in long-lived hydrogen bonds. In contrast, we have previously shown that only the terminal residues of S2-HR2 exhibit fast amide exchange in the presence of cosolvent (*13*). Based on a series of CLEANEX-PM experiments with different mixing times, the k_{ex} of S2-HR2 range from ~3 to 27 s^{-1}. Bai et al. (*31*) have shown that, in the absence of hydrogen bonding, H_N solvent exchange rates vary as a function of amino acid type. Accordingly, we have plotted the relative rates of k_{ex} (k_{ex}/k_{int}) of S2-HR2 in Figure 4b. In this representation, a value near zero would represent an H_N that exhibits a relatively slow k_{ex}, presumably due to participation in a hydrogen bond. Conversely, a value near 1.0 would represent an H_N that exhibits a k_{ex} value approaching the completely exposed value. As shown by Figure 4b, the relative exchange rates do not suggest that the helical structure inferred from CD and NMR ^{13}C chemical shift is protecting H_N (i.e., the helical residues are well exposed due to the equilibrium between structured and unstructured forms of S2-HR2 on the millisecond time scale).

Inhibition of SARS-CoV Entry by S2-HR2. Previous studies of smaller S2-HR2 constructs have suggested that S2-HR2 inhibits SARS-CoV entry, albeit at a relatively poor level with respect to the inhibition of HIV by the analogous HR2 regions (*21–23*). To test the inhibition of SARS-CoV entry, we developed a pseudotyping system. In this system, pseudovirions consisting of S/HIV are formed. S-mediated entry is quantified by luciferase activity. In Figure 5, the entry of S/HIV pseudovirion entry into 293T cells expressing ACE2, the SARS-CoV receptor, is shown as a function of S2-HR2 concentration. The inhibition at the highest S2-HR2 concentration tested, 100 μM, is ~40%, suggesting an IC_{50} value >50 μM. Thus, the present S2-HR2 construct is a relatively poor inhibitor of SARS-CoV entry.

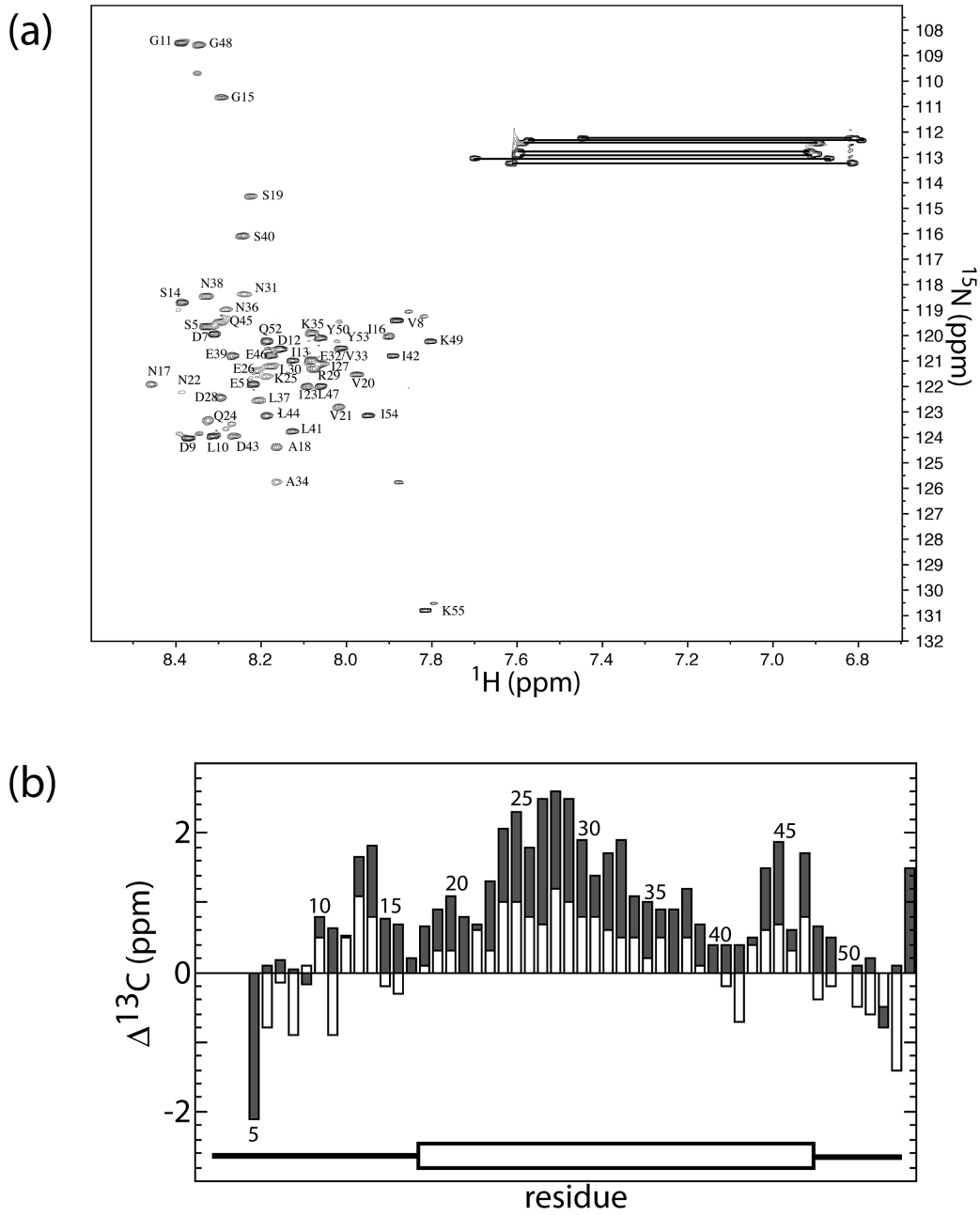

FIGURE 3: NMR assignment and secondary structure of SARS-CoV S2-HR2 under aqueous conditions. (a) ^{15}N-edited HSQC of S2-HR2 acquired on a Bruker 800 MHz spectrometer with a triple-resonance cryoprobe. Horizontal lines connect the side-chain amide pairs of asparagine and glutamine residues. Unlabeled peaks correspond to minor forms of the terminal residues. Sample conditions were 400 μM S2-HR2 monomer, 10 mM $NaPO_4$, pH 7.0, and 10% ^2H_2O at 25 °C. (b) Secondary chemical shift with respect to random coil $^{13}C_\alpha$ (shaded) and ^{13}CO (open) values. Random coil ^{13}C values were taken from Wishart and Case (*32*). The core helix region observed for S2-HR2 in the presence of cosolvent (*13*) is shown at the bottom. Numbering corresponds to that of the construct (cf. Figure 1a).

DISCUSSION

Model for SARS-CoV S2-Mediated Entry. Based on the present observations, a model for SARS-CoV S2-mediated viral entry is presented in Figure 6. In this model three states exist (*1*): a prefusion state in which S2-HR1 and -HR2 domains self-associate to form trimers consisting of coiled coils (*2*); a transition state in which S2-HR2 exists as unstructured monomers (*3*); a postfusion state in which S2-HR2 associates with S2-HR1 to form the six-helix bundle. The existence of the prefusion state is supported by the X-ray structure of S2-HR1 (*16*) and NMR structure (*13*) of S2-HR2. Moreover, the S2-HR1 prefusion state is corroborated by the observation that S2-HR2 peptides inhibit SARS-CoV entry (*22, 23*) (Figure 5). The existence of the postfusion state is substantiated by the X-ray structures of the six-helix bundle (*14–16*). The CD and NMR data presented herein support the existence of S2-HR2 in the transition state. Moreover, the data suggest that there is a dynamic equilibrium between the S2-HR2 in the prefusion and transition states.

An important aspect of this model is that the unstructured transition state enables passage from the prefusion state to the postfusion state. This leads us to speculate that the S2-HR2 domain has evolved to maintain equilibrium between structured and unstructured states, in contrast to intrinsically unstructured domains (*33*). The tendency for S2-HR2 to form

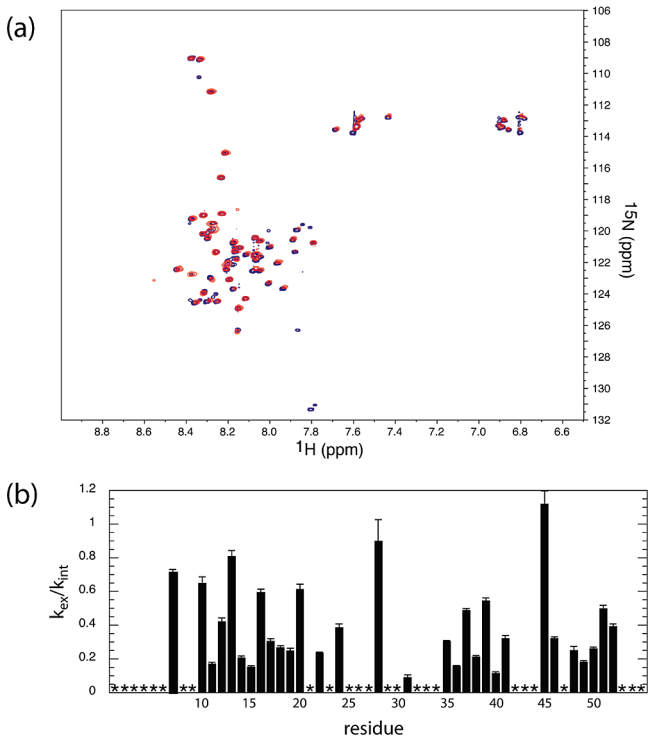

FIGURE 4: Dynamic properties of SARS-CoV S2-HR2. (a) CLEANEX-PM ^{15}N-edited HSQC of S2-HR2 with a mixing time of 100 ms (red) versus the standard ^{15}N-edited HSQC of S2-HR2 (blue). Experimental conditions were 400 μM S2-HR2 in 10 mM $NaPO_4$, pH 7.0, and 10% ^2H_2O at 25 °C. (b) Relative H_N exchange rates from a series of CLEANEX-PM experiments in which the mixing times were 5−100 ms (cf. Materials and Methods). The asterisks denote residues for which k_{ex} could not be determined. The error bars represent the estimated error in determining k_{ex}. Numbering corresponds to that of the construct (cf. Figure 1a).

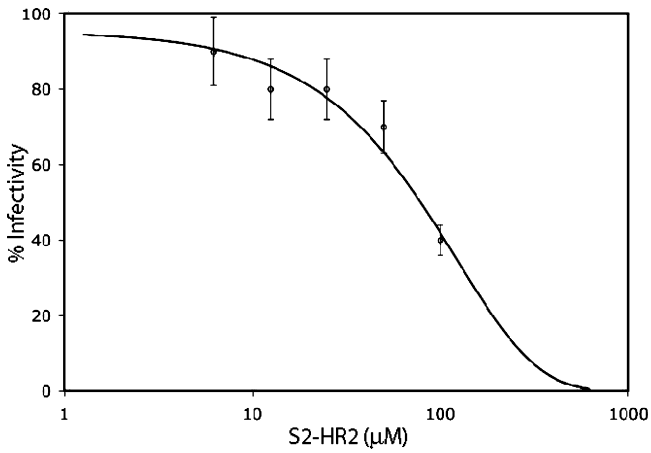

FIGURE 5: Inhibition of pseudovirus harboring SARS-CoV envelope entry by SARS-CoV S2-HR2. The error bars represent the standard deviation of three separate experiments from the transfection step.

a coiled-coil trimer (the prefusion state) suggests that the structured trimer is energetically favored with respect to unstructured monomers (the transition state). On the other hand, previous studies of the SARS-CoV S2 postfusion conformation (i.e., the six-helix bundle), as well as studies of the analogous structures of other viral envelope proteins, imply that the postfusion conformation is the most energetically favored state. Indeed, Tripet et al. have shown that the T_m of SARS-CoV S2-HR1/S2-HR2 is >70 °C (*26*). Thus, the prefusion and transition states correspond to metastable

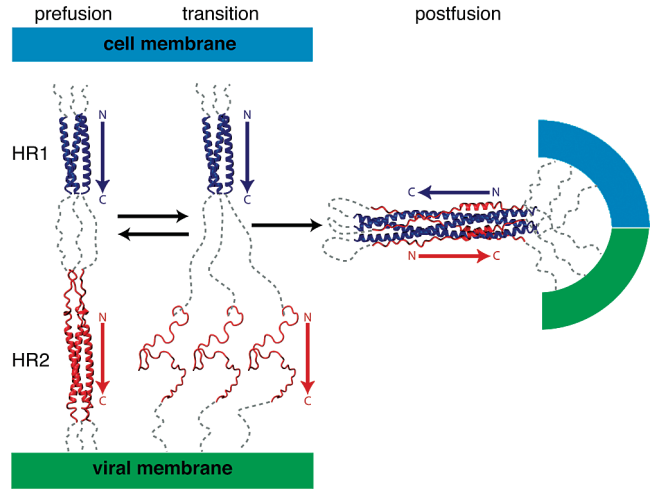

FIGURE 6: Model for the different states of the SARS-CoV S2 fusion protein during viral entry. S2-HR1 and S2-HR2, as well as the direction of the polypeptide chain, are depicted in blue and red, respectively. Dotted gray lines correspond to S2 regions of unknown structure. The position of the viral membrane is deduced from the location of the S2-HR2 C-terminus. The structures for the S2-HR1 (residues 940−973) and S2-HR2 (residues 1141−1193) prefusion states and the S2-HR1/S2-HR2 (residues 896−972/1142−1183) postfusion state have been taken from previous work (*13, 15, 16*). The S2-HR2 transition state was modeled by simulated annealing in the absence of NMR restraints (*13*).

states. It is important to note that viral entry models are primarily based on *in vitro* studies of isolated HR1 and HR2 domains. Consequently, numerous factors present *in vivo* could play important roles in determining the presence and equilibrium of the proposed states including the missing S2 residues, interactions with S1, glycosylation of S2 sites, and membrane anchoring of S2. Nonetheless, the model for SARS-CoV entry may also be applicable to other enveloped viruses. For example, in HIV gp41 and paramyxovirus F, the six-helix bundle, which corresponds to the postfusion state of the model, is very well documented by structural studies. In the case of paramyxovirus, the structure of the prefusion state of the F protein has also been determined (*20*). To date, the presence of the prefusion state of HIV gp41 has eluded characterization by biophysical techniques; however, we note that the prefusion state of paramyxovirus F was only observed upon stabilization of the HR2 coiled-coil domain with the addition of non-native residues that favor the formation of coiled-coil structure. Finally, evidence for the transition state is lacking for paramyxovirus F; however, in the case of HIV gp41, the presence of the transition state of HR2 may be inferred from studies that have shown that it is relatively unstructured in isolation (*34*).

Implications for Antiviral Therapies Based on HR2. The presence of multiple conformational states of HR2 during viral entry has important implications for the design of antiviral or immune-based therapies. In principle, one could target the prefusion and/or transition states of HR2 to disrupt formation of the postfusion state and hence disrupt envelope-mediated fusion of the viral and target membranes, a necessary step in viral entry. For example, a drug, peptide, or antibody that binds to the HR2 helix in the prefusion state could inhibit formation of the postfusion state. However, in cases where a drug or peptide disrupts the HR2 coiled-coil trimer, viral entry may, in fact, be enhanced by favoring the HR2 transition state characterized herein. On the other hand,

premature activation of the HR2 transition state may effectively inhibit viral entry before attachment of the virus to its receptor. Alternatively, stabilization of the prefusion HR2 state may be expected to inhibit viral entry by prohibiting formation of the transition state. Taken together, the multiple structural states of viral envelope, which are in dynamic equilibrium, underscore the challenges faced in the design of viral entry inhibitors.

REFERENCES

1. Colman, P. M., and Lawrence, M. C. (2003) The structural biology of type I viral membrane fusion. *Nat. Rev. Mol. Cell Biol. 4*, 309–319.
2. Chan, D. C., and Kim, P. S. (1998) HIV entry and its inhibition. *Cell 93*, 681–684.
3. Skehel, J. J., and Wiley, D. C. (2000) Receptor binding and membrane fusion in virus entry: the influenza hemagglutinin. *Annu. Rev. Biochem. 69*, 531–569.
4. Hofmann, H., and Pohlmann, S. (2004) Cellular entry of the SARS coronavirus. *Trends Microbiol. 12*, 466–472.
5. Burkhard, P., Stetefeld, J., and Strelkov, V. (2001) Coiled coils: a highly versatile protein folding motif. *Trends Cell Biol. 11*, 82–88.
6. Caffrey, M., Cai, M., Kaufman, J., Stahl, S. J., Wingfield, P. T., Covell, D. G., Gronenborn, A. M., and Clore, G. M. (1998) Three-dimensional solution structure of the 44 kDa ectodomain of SIV gp41. *EMBO J. 17*, 4572–4584.
7. Chan, D. C., Fass, D., Berger, J. M., and Kim, P. S. (1997) Core structure of gp41 from the HIV envelope glycoprotein. *Cell 89*, 263–273.
8. Tan, K., Liu, J., Wang, J., Shen, S., and Lu, M. (1997) Atomic structure of a thermostable subdomain of HIV-1 gp41. *Proc. Natl. Acad. Sci. U.S.A. 94*, 12303–12308.
9. Weissenhorn, W., Dessen, A., Harrison, S. C., Skehel, J. J., and Wiley, D. C. (1997) Atomic structure of the ectodomain from HIV-1 gp41. *Nature 387*, 426–430.
10. Wilson, I. A., Skehel, J. J., and Wiley, D. C. (1981) Structure of the haemagglutinin membrane glycoprotein of influenza virus at 3 Å resolution. *Nature 289*, 366–373.
11. Bullough, P. A., Hughson, F. M., Skehel, J. J., and Wiley, D. C. (1994) Structure of influenza haemagglutinin at the pH of membrane fusion. *Nature 371*, 37–43.
12. Gamblin, S. J., Haire, L. F., Russell, R. J., Stevens, D. J., Xiao, B., Ha, Y., Vasisht, N., Steinhauer, D. A., Daniels, R. S., Elliot, A., Wiley, D. C., and Skehel, J. J. (2004) The structure and receptor binding properties of the 1918 influenza hemagglutinin. *Science 303*, 1838–1842.
13. Hakansson-McReynolds, S., Jiang, S., Rong, L., and Caffrey, M. (2006) The solution structure of the severe acute respiratory syndrome-coronavirus heptad repeat 2 in the prefusion state. *J. Biol. Chem. 281*, 11965–11971.
14. Xu, Y., Lou, Z., Liu, Y., Pang, H., Tien, P., Gao, G. F., and Rao, Z. (2004) Crystal structure of severe acute respiratory syndrome coronavirus spike protein fusion core. *J. Biol. Chem. 279*, 49414–49419.
15. Supekar, V. M., Bruckmann, C., Ingallinella, P., Bianchi, E., Pessi, A., and Carfí, A. (2004) Structure of a proteolytically resistant core from the severe acute respiratory syndrome coronavirus S2 fusion protein. *Proc. Natl. Acad. Sci. U.S.A. 101*, 17958–17963.
16. Deng, Y., Liu, J., Zheng, Q., Yong, W., and Lu, M. (2006) Structures and polymorphic interactions of two heptad-repeat regions of the SARS virus S2 protein. *Structure 14*, 889–899.
17. Malashkevich, V. N., Schneider, B. J., McNally, M. L., Milhollen, M. A., Pang, J. X., and Kim, P. S. (1999) Core structure of the envelope glycoprotein GP2 from Ebola virus at 1.9-Å resolution. *Proc. Natl. Acad. Sci. U.S.A. 96*, 2662–2667.
18. Weissenhorn, W., Carfi, A., Lee, K. H., Skehel, J. J., and Wiley, D. C. (1998) Crystal structure of the Ebola virus membrane fusion subunit, GP2, from the envelope glycoprotein ectodomain. *Mol. Cell 2*, 605–616.
19. Yin, H. S., Paterson, R. G., Wen, X., Lamb, R. A., and Jardetzky, T. S. (2005) Structure of the uncleaved ectodomain of the paramyxovirus (hPIV3) fusion protein. *Proc. Natl. Acad. Sci. U.S.A. 102*, 9288–9293.
20. Yin, H. S., Wen, X., Paterson, R. G., Lamb, R. A., and Jardetzky, T. S. (2006) Structure of the parainfluenza virus 5 F protein in its metastable, prefusion conformation. *Nature 439*, 38–44.
21. Wild, C., Shugars, D., Greenwell, T., McDanal, C., and Matthews, T. (1994) Peptides corresponding to a predictive α-helical domain of human immunodeficiency virus type 1 gp41 are potent inhibitors of virus infection. *Proc. Natl. Acad. Sci. U.S.A. 91*, 9770–9774.
22. Bosch, B. J., Martina, B. E., Van Der Zee, R., Lepault, J., Haijema, B. J., Versluis, C., Heck, A. J., De Groot, R., Osterhaus, A. D., and Rottier, P. J. (2004) Severe acute respiratory syndrome coronavirus (SARS-CoV) infection inhibition using spike protein heptad repeat-derived peptides. *Proc. Natl. Acad. Sci. U.S.A. 101*, 8455–8460.
23. Liu, S., Xiao, G., Chen, Y., He, Y., Niu, J., Escalante, C. R., Xiong, H., Farmar, J., Debnath, A. K., Tien, P., and Jiang, S. (2004) Interaction between heptad repeat 1 and 2 regions in spike protein of SARS-associated coronavirus: implications for virus fusogenic mechanism and identification effusion inhibitors. *Lancet 363*, 938–947.
24. Kilby, J. M., Lalezari, J. P., Eron, J. J., Carlson, M., Cohen, C., Arduino, R. C., Goodgame, J. C., Gallant, J. E., Volberding, P., Murphy, R. L., Valentine, F., Saag, M. S., Nelson, E. L., Sista, P. R., and Dusek, A. (2002) The safety, plasma pharmacokinetics, and antiviral activity of subcutaneous enfuvirtide (T-20), a peptide inhibitor of gp41-mediated virus fusion, in HIV-infected adults. *AIDS Res. Hum. Retroviruses 18*, 685–693.
25. Bosch, B. J., van der Zee, R., de Haan, C. A., and Rottier, P. J. (2003) The coronavirus spike protein is a class I virus fusion protein: structural and functional characterization of the fusion core complex. *J. Virol. 77*, 8801–8811.
26. Tripet, B., Howard, M. W., Jobling, M., Holmes, R. K., Holmes, K. V., and Hodges, R. S. (2004) Structural characterization of the SARS-coronavirus spike S fusion protein core. *J. Biol. Chem. 279*, 20836–20849.
27. Schuck, P. (2000) Size-distribution analysis of macromolecules by sedimentation velocity ultracentrifugation and Lamm equation modeling. *Biophys. J. 78*, 1606–1619.
28. Delaglio, F., Grzesiek, S., Vuister, G., Zhu, G., Pfeifer, J., and Bax, A. (1995) NMRPipe: a multidimensional spectral processing system based on UNIX pipes. *J. Biomol. NMR 6*, 277–293.
29. Mori, S., Abeygunawardana, C., van Zijl, P., and Berg, J. (1996) Water exchange filter with improved sensitivity (WEX II) to study solvent-exchangeable protons. Application to the consensus zinc finger peptide CP-1. *J. Magn. Reson. 110*, 96–101.
30. Hwang, T. L., van Zijl, P. C., and Mori, S. (1998) Accurate quantitation of water-amide proton exchange rates using the phase-modulated CLEAN chemical EXchange (CLEANEX-PM) approach with a Fast-HSQC (FHSQC) detection scheme. *J. Biomol. NMR 11*, 221–226.
31. Bai, Y., Milne, J., Mayne, L., and Englander, S. (1993) Primary structure effects on peptide group hydrogen exchange. *Proteins 17*, 75–86.
32. Wishart, D. S., and Case, D. A. (2001) Use of chemical shifts in macromolecular structure determination. *Methods Enzymol. 338*, 3–34.
33. Dyson, H. J., and Wright, P. E. (2005) Intrinsically unstructured proteins and their functions. *Nat. Rev. 6*, 197–208.
34. Lu, M., Blacklow, S. C., and Kim, P. S. (1995) A trimeric structural domain of the HIV-1 transmembrane glycoprotein. *Nat. Struct. Biol. 2*, 1075–1082.

BI800622T